Article

Magnetically Stimulable Graphene Oxide/Polypropylene Nanocomposites

Muhammad Nisar,* Griselda Barrera Galland, Julian Geshev, Carlos Bergmann, and Raúl Quijada*

Read Online

ACCESS | Metrics & More | Article Recommendations

ABSTRACT: Core−shell magnetic air-stable nanoparticles have attracted increasing interest in recent years. Attaining a satisfactory distribution of magnetic nanoparticles (MNPs) in polymeric matrices is difficult due to magnetically induced aggregation, and supporting the MNPs on a nonmagnetic core−shell is a well-established strategy. In order to obtain magnetically active polypropylene (PP) nanocomposites by melt mixing, the thermal reduction of graphene oxides (TrGO) at two different temperatures (600 and 1000 °C) was carried out, and, subsequently, metallic nanoparticles (Co or Ni) were dispersed on them. The XRD patterns of the nanoparticles show the characteristic peaks of the graphene, Co, and Ni nanoparticles, where the estimated sizes of Ni and Co were 3.59 and 4.25 nm, respectively. The Raman spectroscopy presents typical D and G bands of graphene materials as well as the corresponding peaks of Ni and Co nanoparticles. Elemental and surface area studies show that the carbon content and surface area increase with thermal reduction, as expected, following a reduction in the surface area by the support of MNPs. Atomic absorption spectroscopy demonstrates about 9−12 wt % metallic nanoparticles supported on the TrGO surface, showing that the reduction of GO at two different temperatures has no significant effect on the support of metallic nanoparticles. Fourier transform infrared (FT-IR) spectroscopy shows that the addition of a filler does not alter the chemical structure of the polymer. Scanning electron microscopy of the fracture interface of the samples demonstrates consistent dispersion of the filler in the polymer. The TGA analysis shows that, with the incorporation of the filler, the initial (T_{onset}) and maximum (T_{max}) degradation temperatures of the PP nanocomposites increase up to 34 and 19 °C, respectively. The DSC results present an improvement in the crystallization temperature and percent crystallinity. The filler addition slightly enhances the elastic modulus of the nanocomposites. The results of the water contact angle confirm that the prepared nanocomposites are hydrophilic. Importantly, the diamagnetic matrix is transformed into a ferromagnetic one with the addition of the magnetic filler.
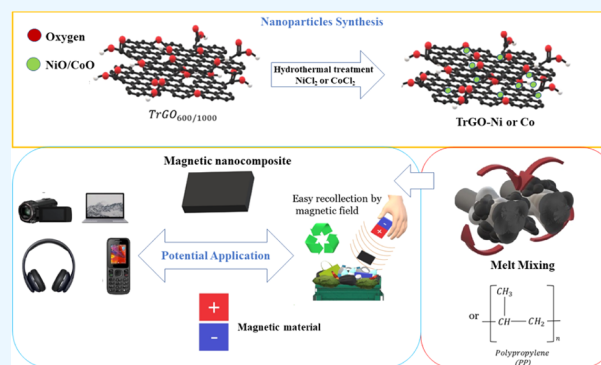
1. INTRODUCTION

Stimuli-responsive materials that can effectively respond to external incentives, for instance, electrical or magnetic fields, alterations in temperature, or mechanical force, have recently become a hot topic of research in materials science.[1] In this respect, in the last few decades, nanofiller-reinforced polymer composites have attracted significant interest in a large number of applications, including energy storage, biomedical, automotive, aerospace, computing, construction, astronomy, and other fields.[2,3] The incorporation of carbon nanostructures to synthesize polymeric nanocomposites with improved mechanical properties and/or electrical conductivity is a promising alternative. The electrically insulated and soft polymeric matrix imparts mechanical resistance, and the carbon nanomaterials provide electrical conductivity.[4] The discovery of monolayer graphene, presenting a hexagonal lattice arrangement composed of sp²-hybridized carbon atoms, has opened a wide range of research possibilities. The excellent thermal, mechanical, electrical, and various other properties make

graphene a suitable material for sensors, electronics, catalysis, drug delivery, and energy devices.[5−8] The cutting-edge utilization of graphene is its use as a reinforcement in polymer matrices due to its exceptional characteristics, including superior mechanical strength, thermal conductivity, and surface area.[6,9]

Nanofiller-reinforced polymer nanocomposites have gained increasing attention from researchers both in academic and industrial sectors due to the significant enhancement in their mechanical, thermal, and flame retardancy properties at low filler loadings. The incorporation of nanofillers in polymers,
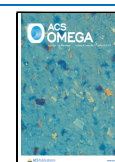
namely, inorganic nanoparticles (Ag, TiO$_2$, ZnO, etc.), layered silicates, and carbon nanostructures (nanofibers (CNFs), nanotubes (CNTs) fluorenes, graphene, etc.), has demonstrated substantial improvement in properties at very low filler loadings compared to microfiller-reinforced polymers.[3,10] Because of the exceptionally high strength, electrical conductivity, and abundant presence of the precursor "graphite", graphene is of particularly great interest in the advancement of graphene polymer nanocomposites.[11,12] The oxidation of naturally abundant graphite flakes leads to the formation of 2D lamellae of graphene oxide (GO), containing extensive hydrophilic functionalities, such as carbonyl, hydroxyl, epoxide, ester, ether, and carboxylic groups.[13] A GO surface that accommodates oxygen functionalities is very interesting as it offers interaction sites with the polymer matrix.[14] In addition, the high surface area of graphene makes it a fascinating hosting material, which allows the dispersion of different nanoparticles (NPs) on its surface with special properties, such as magnetic nanoparticles.

Several GO–polymer nanocomposites have been reported using different polymers, for instance, polycarbonates, polydimethyl siloxane, poly (vinylalcohol), polyurethane, polymethylmethacrylate, and polyolefins.[15−19] PP is one of the commercially important nonpolar semicrystalline polyolefins; its light weight, cost-effectiveness, and easy processability make it the material of choice for a wide variety of industrial applications. The incorporation of GO significantly enhances the mechanical, gas barrier, and thermal conductivity properties, as well as introduces electrical conductivity into the insulating PP matrix.[20,21] However, to the best of the authors' knowledge, few studies have been reported on multifunctional magnetic PP nanocomposites.

Recently, core–shell air-stable MNPs have gained considerable interest because of their promising applications in biotechnology, medicine, tissue engineering, water treatment, data storage, and catalysis.[22−25] The combination of a magnetic core with the possibility to functionalize its surface is an important benefit of these materials. The protection of the metallic nanomagnet by an additional protective layer that is inert toward acids and air and thermally stable guarantees a considerably higher magnetic moment. A variety of protective coatings, such as silica, carbon, transition metal oxides, and gold, have been proposed.[26−28] Because of the high cost, gold is not considered as an appropriate choice; the hydrolysis of covalent bonds on metal oxides and silica makes them less desirable, thus promoting carbon coatings as the most preferred choice. Iron is a conventional magnetic filler commonly introduced to afford magnetism, along with cobalt and nickel.[29,30] On the other hand, the magnetic properties of the finally produced composites are greatly affected/limited by various factors, specifically, the extent of dispersion/agglomeration, interparticle interaction, and surface effect on the magnetism of the nanoparticles.[31] Nanoparticles usually tend to form agglomerates; the situation is more complex in the case of magnetic nanoparticles (MNPs) as magnetically induced aggregates are formed. Therefore, it is imperative to support the MNPs on the surface of nonmagnetic materials for effective dispersion and to attain the desired properties of the polymeric nanocomposites.

Melt mixing is considered as the most adequate industrial-scale process for polymer composite production due to its cost-effectiveness, fast production rate, environmentally friendly nature, simple operation, and high yield. Thus, in the present work, graphene oxides thermally reduced at 600 and 1000 °C (TrGO) were synthesized, and metallic nanoparticles of either nickel (Ni) or cobalt (Co) were supported on them. Magnetic and structural properties of the Ni and Co supported on TrGO were studied. Furthermore, PP and TrGO-M (M = Ni, Co) were melt-mixed in order to determine the impact of the incorporation of these stimuli-responsive nanofillers on the properties of the PP matrix.

2. EXPERIMENTAL SECTION

2.1. Materials. Graphite, hydrochloric acid (HCl, 37%), sodium nitrate (NaNO$_3$; 99.0% purity), sulfuric acid (H$_2$SO$_4$; 98% purity), pure potassium permanganate (KMnO$_4$; ≥99.0% purity), and cobalt (II) chloride (CoCl$_2$) were purchased from Merck (Kenilworth, NJ). Nickel (II) chloride hexahydrate (NiCl$_2$·6H$_2$O) was supplied by Quimica Fina (Bogota D.C) and hexamethylenetetramine (C$_6$H$_{12}$N$_4$) by Labsynth (Diadema, SP). Polypropylene (PP) PH 2621, having a molecular weight of 195 Kg·mol^{-1}, a density of 905 kg·m^{-3}, and a melt flow index of 27 g/10 min (2.16 kg, 230 °C), was purchased from Petroquim S.A and used as received.

2.2. Synthesis and Thermal Reduction of Graphene Oxide. The modified Hummers method was used to synthesize graphene oxide (GO). Initially, 375 mL of H$_2$SO$_4$ at 0 °C was used to disperse 7.5 g of NaNO$_3$ and 15 g of graphite under constant stirring. After 30 min of stirring, 45 g of KMnO$_4$ was added over a period of 4 h. The suspension was left at 25 °C for a further 45 min to react. The suspension was slowly poured into a solution containing 675 mL of hydrogen peroxide (5 vol %) and 750 mL of distilled water to eliminate additional KMnO$_4$. The synthesized material was cleaned with HCl (26%) followed by washing with distilled water numerous times to achieve a pH of *ca.* 7. Lastly, the drying of GO at 80 °C was carried for 1 h.[32]

Before the thermal reduction of GO to obtain TrGO, 6 h of vacuum drying was performed at 80 °C. A calculated small amount of GO was placed in a quartz rector, closed, and purged with nitrogen gas. The process of thermal reduction was carried out at either 600 or 1000 °C for ~30 s. Finally, the reactor was cooled to room temperature to collect TrGO. To achieve the exfoliation and reduction of graphene sheet functional groups, thermal shocking is considered as the main prerequisite.[33]

2.3. Support of Metallic Nanoparticles on the TrGO Surface. The dispersion of MNPs on the surface of TrGO was carried out by ultrasonic dispersion of 1.0 g of TrGO in 250 mL of distilled water. Similarly, hexamethylenetetramine (HMT; 4.8 mmol) and NiCl$_2$·6H$_2$O (2.4 mmol) were separately dissolved in 170 and 70 mL of water, respectively, to maintain a 1:2 molar ratio. Furthermore, all three solutions were shifted to a round-bottom flask under overnight stirring. The final solution is subjected to hydrothermal reaction using a Teflon-lined stainless steel autoclave for 4 h at 120 °C to obtain TrGO-supported Ni(OH)$_2$. To remove the excess Ni and HMT, the obtained black powder was washed and filtered numerous times. Finally, the TrGO-supported Ni(OH)$_2$ was heated in air up to 380 °C for 60 min to obtain crystalline NiO-supported TrGO.[34] A similar process with similar concentrations was used to support cobalt nanoparticles on the TrGO surface using CoCl$_2$.

2.4. Preparation of Polypropylene TrGO–Metal Nanoparticle Nanocomposites. PP-TrGO nanocomposites were synthesized using a Brabender Plasticorder double screw
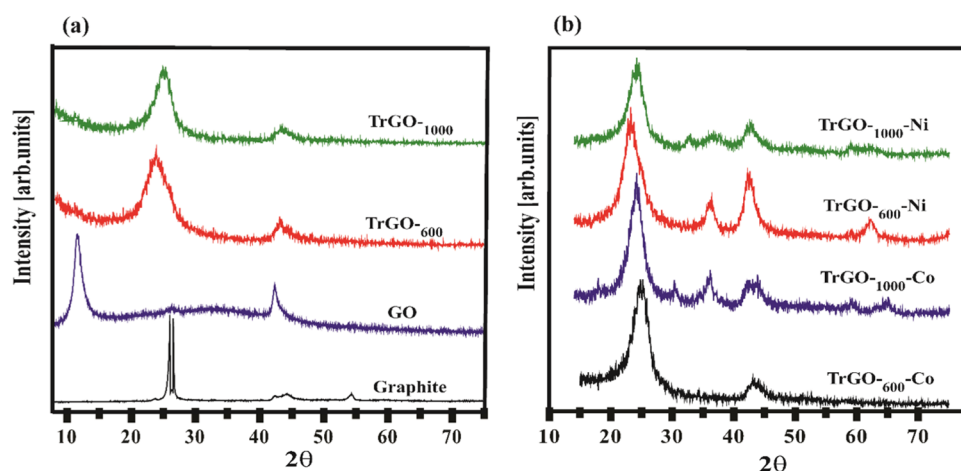
Figure 1. XRD patterns of neat graphite, GO, and TrGO at 600 and 1000 °C (a) and TrGO-supporting Ni and Co nanoparticles (b).

mixer (Nordrhein-Westfalen, Germany). TrGO-containing metallic nanoparticles (Ni, Co) and PP were dried at 80 °C for 8h before mixing. Initially, the PP matrix was melted at 190 °C for 3 min. Subsequently, TrGO-containing metallic nanoparticles were added to a mixing chamber, and the rotor speed was maintained at 110 rpm for a total time period of 10 min. The quantity of the filler in the prepared composites differed from 1 to 5 wt %. Finally, the nanocomposite films were prepared by processing at 190 °C in a hydraulic press having a water-cooling apparatus. The prepared films have a thickness of 1.0 mm for measurements.

3. CHARACTERIZATION

The analysis of the specific surface area and pore structure parameters of the GO, TrGO, and TrGO-supported metallic nanoparticles was performed at −196 °C by obtaining the nitrogen adsorption−desorption isotherms using a Micromeritics Instrument, TriStar II 3020. The pore size distribution (PSD) was calculated by the Barrett−Joyner−Halenda (BJH) method using the adsorption branch. A 16 h outgassing of the samples at 200 °C was carried out before measurements.

The carbon, nitrogen, hydrogen, and oxygen contents of the synthesized nanoparticles were determined using an elemental analyzer (Perkin Elmer M CHNS/O model 2400). The C, N, and H percentages were subtracted from the total mass to derive the oxygen percentage.

The morphological analysis was carried out by field-emission scanning electron microscopy in the secondary electron mode using the Inspect F50 equipment (FEI Instruments). An aluminum stub was used to place the samples, and gold coating was performed to make it a conductor.

The phase compositions of neat nanoparticles and Ni- and Co-supported nanoparticles were assessed by X-ray diffractometry (XRD), using a Philips Diffractometer, X'Pert MPD model, accompanied by a fixed anode and graphite monochromator run at 40 kV and 40 mA using Cu-Ka radiation. Raman spectroscopy was performed to evaluate the structural characteristics of the synthesized nanoparticles using a classical Renishaw Raman spectroscope inVia spectrometer system. The experiment was carried out in the range of 0 to 3100 cm^{-1} using a 514 nm laser at room temperature. Fourier transform infrared (FT-IR) spectroscopy was performed for structural analysis. A Perkin Elmer spectrum 100 spectrometer

was used to record the FT-IR spectra using attenuated total reflection mode ranging from 4000 to 400 cm^{-1}.

A high-resolution atomic absorption spectrometer with the model contraAA 700 (Analytik Jena AG, Jena, Germany) equipped with a flame atomizer (HR-CS F AAS) and continuum source graphite furnace (HR-CS GF AAS) was used for the quantification of metal nanoparticles supported on the TrGO surface. The direct sample weighing method was applied to the graphite platform, with masses ranging from 0.10 to 0.16 mg. A preadapted pair of tweezers was used for the transference of the pyrolytically coated graphite tubes to the atomizer. The reported method and program temperature were adapted from the literature.[35] Before the introduction of the graphite tube into the atomizer, the sample was treated with a 10 mL chemical modifier prepared by mixing 12 mg of Mg and 20 mg of Pd. Pyrolysis and atomization were carried out at temperatures of 800 and 2500 °C, respectively.

Thermal analysis of the polymer nanocomposites was carried out by differential scanning calorimetry (DSC) and thermogravimetric analysis (TGA). A DSC model Q20 of Perkin Elmer differential calorimeter at a heating rate of 10 °C/min was used, in the range of 0−180 °C. The crystallinity percent was obtained using the enthalpy of fusion data calculated from the DSC curves, and the melting temperature (T_m) was determined from the second scan. The thermal stability and percent residue of the samples in comparison to those of pure PP were calculated by a Q20 SDT Q600 thermal analyzer at a scanning rate of 10 °C/ min from 0 to 700 °C.

The ASTMD 638-10 method was applied to measure the stress−strain curve of the neat PP and its nanocomposites using a dynamometer HP model D-500 at ~25 °C. Five measurements were carried out for each wt % of the sample using a speed of 50 mm min^{-1}; the presented results are the average of five measurements. The water contact angle (WCA) was measured by a goniometer (Phoenix 300, SEO) using the sessile drop method. Each sample was subjected to five drops of water, and the angle calculated was the mean of the five tests; "a drop shape analysis system" was used to obtain images taking into account an experimental error of 2.

Magnetic moments of the nanoparticles and the magnetic filler-filled polymer were studied by applying a magnetic field. An EZ9 MicroSense vibrating sample magnetometer (VSM) was used at room temperature, with a magnetic field (H) of up to 20 kOe. The room temperature variation of H between +20
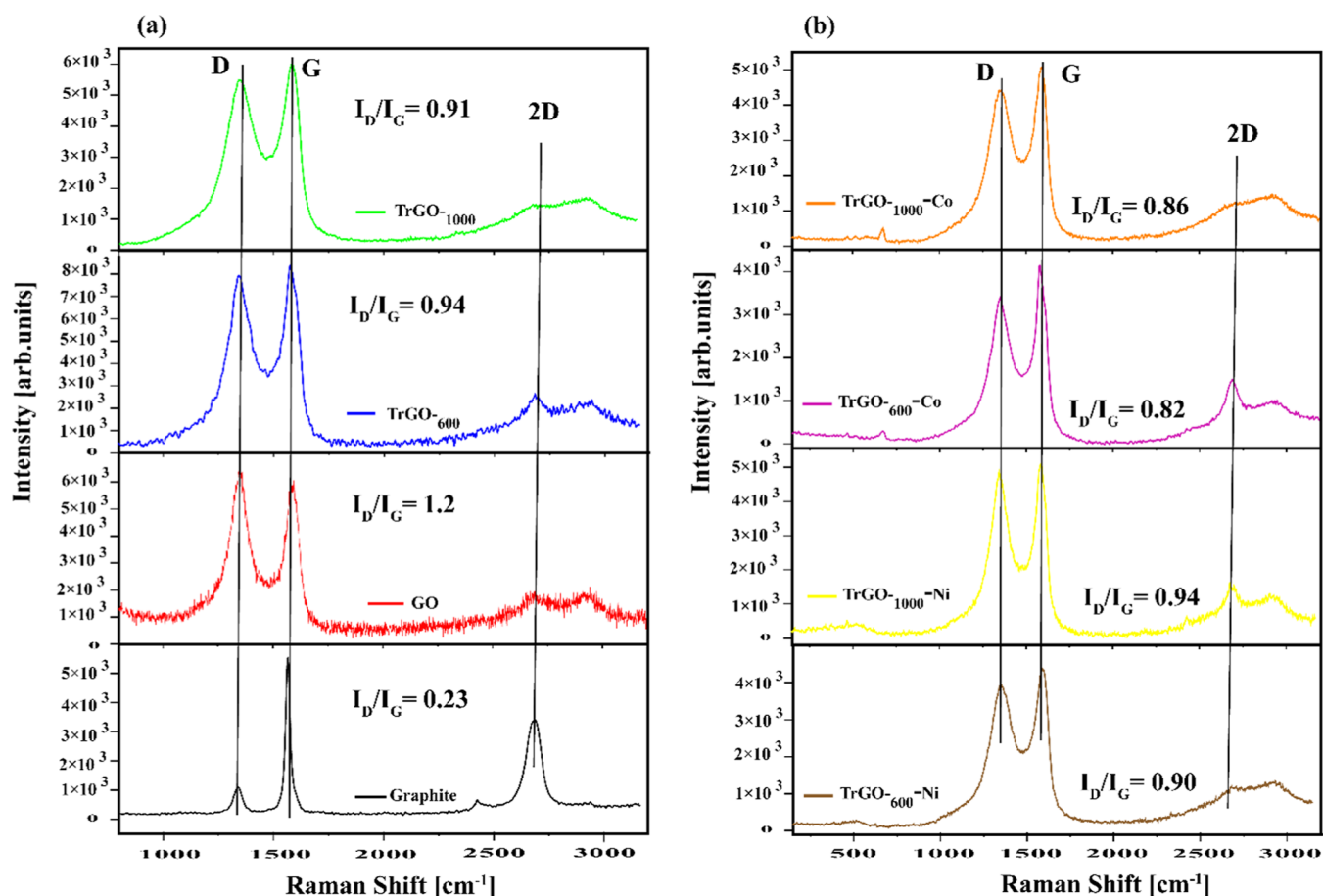
Figure 2. Raman spectra of neat graphite, GO, and TrGO at 600 and 1000 °C (a) and TrGO-supported Ni and Co nanoparticles (b).

and −20 kOe was applied to obtain the hysteresis of magnetization.

4. RESULTS AND DISCUSSION

To assess GO and metallic nanoparticles decorated on TrGO, numerous characterizations were performed. XRD graphs of neat graphite and GO are displayed in Figure 1a. Neat graphite shows a strong diffraction peak at $2\theta = 26.3°$ and a mild peak at 54.5° corresponding to the (002) and (004) planes, respectively. After the oxidation, the peak associated with the (002) plane shifted to a new position ($2\theta = 11.2°$). The change of the peak position to a small angle in the XRD patterns proves the increase in the d-spacing between graphene sheets. The Braggs law and curve fittings were applied to calculate the 2θ and d-spacing values for nanoparticles.[32] It can be concluded that the introduction of oxygen functionalities, for instance, -COOH and -OH, due to the oxidation process increased the d-spacing of pristine graphite from 0.338 to 0.790 nm for GO.[15,36] In contrast, in Figure 1A, the diffractogram of thermally reduced GO at 600 and 1000 °C presents a broad peak, shifted to $2\theta = 23.8$ and 25.1°, respectively, presenting a decrease in the interlayer spacing of the graphene sheets, showing that GO was successfully reduced.[37]

Furthermore, the TrGO-supporting metallic nanoparticles were also characterized by XRD, as shown in Figure 1b. The existence of XRD peaks (in the TrGO$_{600}$-Ni and TrGO$_{1000}$-Ni samples) at $2\theta = 36.7$, 43.2, and 62.3 analogous to the (111), (200), and (220) plane reveals the presence of NiO nanoparticles (JCPDS. 01-078-0429) with a cubic symmetry

$Fm\overline{3}m$.[38] The MNPS average crystalline size was estimated using the Scherer equation.[39] The calculated crystal size of the NiO nanoparticles was 3.59 nm, taking into account the enlargement of the maximum concentrated peak at 36.7° (200 plane). Similarly, Figure 1b shows the XRD pattern of the TrGO$_{600}$-Co and TrGO$_{1000}$-Co samples, where diffraction peaks were observed at $2\theta = 31.1$, 36.7, 44.4, 59.3, and 65.4 associated with the (220), (311), (222), (511), and (440) planes, respectively, identical to the values of JCPDS 01-080-1533, presenting a simple cubic structure of the cobalt oxide.[40] The obtained crystalline size of Co_3O_4 was 4.25 nm considering the intense peak at 36.7° (311), assuming that the XRD study shows a nanometric crystalline structure of the MNPs. In addition, no information on the $Ni(OH)_2$ and $Co(OH)_2$ peaks was obtained, proving the complete transfer of metallic hydroxide to the metallic oxide by annealing at 380 °C. However, the sample TrGO$_{600}$-Co presents only the characteristic peaks of TrGO at $2\theta = 25.1(002)$ and 43.4(222), signifying that the TrGO surface probably has a lower amount of cobalt oxide.

The GO reduction and formation of TrGO-immobilized MNPs were additionally followed by Raman spectroscopy. Figure 2 presents the Raman spectra of neat graphite, GO, and TrGO at 600 and 1000 °C. Two distinct peaks were observed in each spectrum, corresponding to D and G bands. The intensity of the D band (related to the structural defects) of the GO peak is higher than that of TrGO, showing the presence of an additional functional group with sp³ bonds of the graphite basal plane. In contrast, the G band corresponding to the sp²
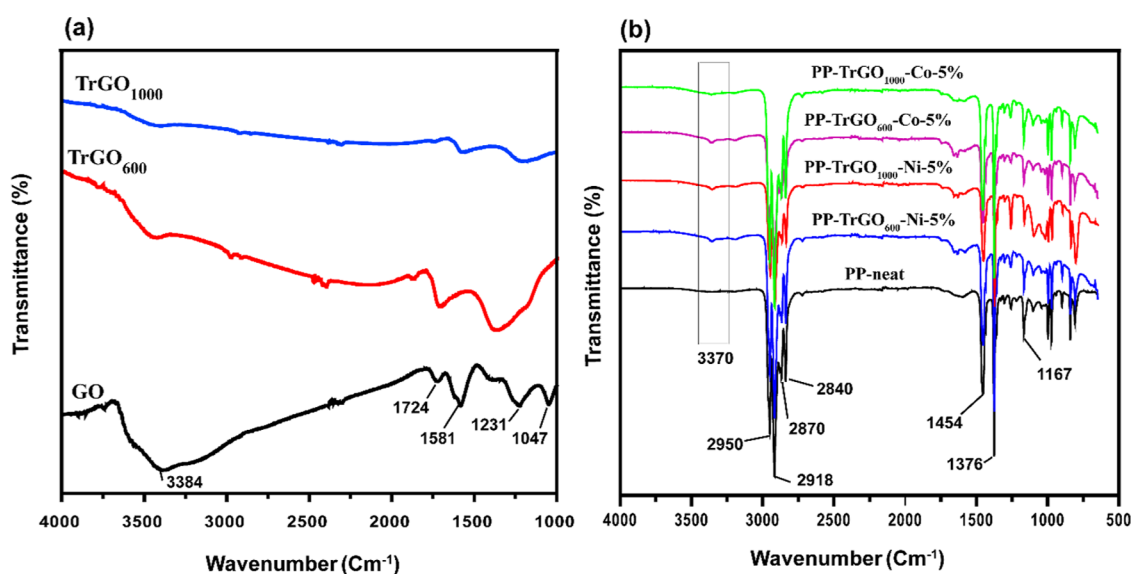
Figure 3. FT-IR spectra of GO and TrGO (a) and the PP nanocomposite (b).

Table 1. Elemental Analysis, Metal Amount, and BET Surface Area

samples	% C	% H	% N	%O	M-content $(\%)^a$	S_{BET} (m^2g^{-1})	V_{tot} $(cm^3\ g^{-1})$
GO	54.4	1.9	0.1	43.6		70	
TrGO$_{600}$	83.9	0.3	0.1	15.7		282	0.572
TrGO$_{1000}$	90.8	0.4	0.1	8.7		373	0.725
TrGO$_{600}$-Co	71.84	0.48	0.41	27.3	9.0 ± 3	147	0.264
TrGO$_{1000}$-Co	72.93	0.65	0.42	26.0	9.0 ± 1	134	0.268
TrGO$_{600}$-Ni	63.94	0.61	0.71	34.74	12 ± 2	186	0.327
TrGO$_{1000}$-Ni	72.9	0.54	0.61	25.95	8.0 ± 2	138	0.231

^{a}Calculated by atomic absorption; S_{BET} = BET surface area; V_{tot} = total pore volume.

carbon−carbon double bond shows higher intensity for TrGO compared to GO. Another parameter to assess the removal of defects and restoration of carbon−carbon double bonds is the I_D/I_G value, which is the intensity ratio of D and G bands. Pure graphene has a well-ordered structure with no defects and is characterized by a low I_D/I_G value.[41] Interestingly, Figure 2a,b shows that the TrGO (reduced at 600 and 1000 °C) spectrum has an inferior intensity of the D band and superior intensity of the G band in comparison to GO, showing a lower I_D/I_G value. These results prove the decrease in the number of structural defects, leading to an increase in sp^2 double bonds, promoting graphene structural renovation by the thermal reduction process.

Furthermore, all samples supported Ni and Co nanoparticles, as expected, showing the typical D and G bands of graphene materials at 1350 and 1585 cm^{-1}, as can be seen in Figure 2b. Moreover, the TrGO-supported Co nanoparticles show peaks around 467, 511, and 672 cm^{-1} attributed to the F_m^{12}, F_g^{22}, and A_{1g} active modes of Co$_3$O$_4$.[42,43] In addition, TrGO-immobilized Ni nanoparticles exhibit Raman bands situated at ∼515 and 618 cm^{-1} ascribed to the $A_{2u}(T)$ lattice vibration of the NiO nanoparticles on the reduced graphene oxide surface. This proves the successful immobilization of metallic NPs on the TrGO surface.[44−47]

FT-IR is a powerful technique to verify the existence of diverse functionalities in the GO structure, as well as to detect oxygen-containing functional groups. Figure 3a displays the FT-IR spectrum of graphene oxide and thermally reduced GO at 600 and 1000 °C; the obtained spectrum of graphene oxide

established the effective oxidation of graphite. The GO spectrum confirms the peaks at 1047, 1231, and 1581 cm^{-1} corresponding to the C−O, C−O−C, and C−OH bendings, respectively. The peak at 1724 cm^{-1} is attributed to the C═O stretching due to the presence of carbonyl groups in the graphene structure. A broad absorption peak at 3384 cm^{-1} corresponds to the O−H stretching, because of the existence of alcohol groups and water molecules overlaid on the OH bending of COOH groups.[48,49]

FT-IR spectra of TrGO at 600 and 1000 °C are also displayed in Figure 3a. One can note that the peak intensities conforming to oxygen functionalities decreased or vanished after GO was thermally reduced. This demonstrates the efficacious reduction of graphene oxide by thermal treatment. However, the complete disappearance of the peaks was not absorbed, indicating a partial reduction of GO by heat treatment.[50]

Table 1 demonstrates the effect of thermal reduction on the chemical composition of graphene oxide (GO). It can be noted from the elemental analysis that the carbon content of GO is 54.4%, which gradually increased to 83.9 and 90.8% by the thermal reduction at 600 and 1000 °C, respectively. Similarly, a significant decrease in the oxygen content from 43.6 to 15.7% and 8.70% is observed by reducing GO at 600 and 1000 °C, respectively. TrGO$_{1000}$ shows the lowest content of oxygen, attributed to the higher temperature during the reduction process promoting a more complete reduction of GO. On the other hand, the support of the metallic nanoparticles on the TrGO surface shows a slight decrease in the carbon content
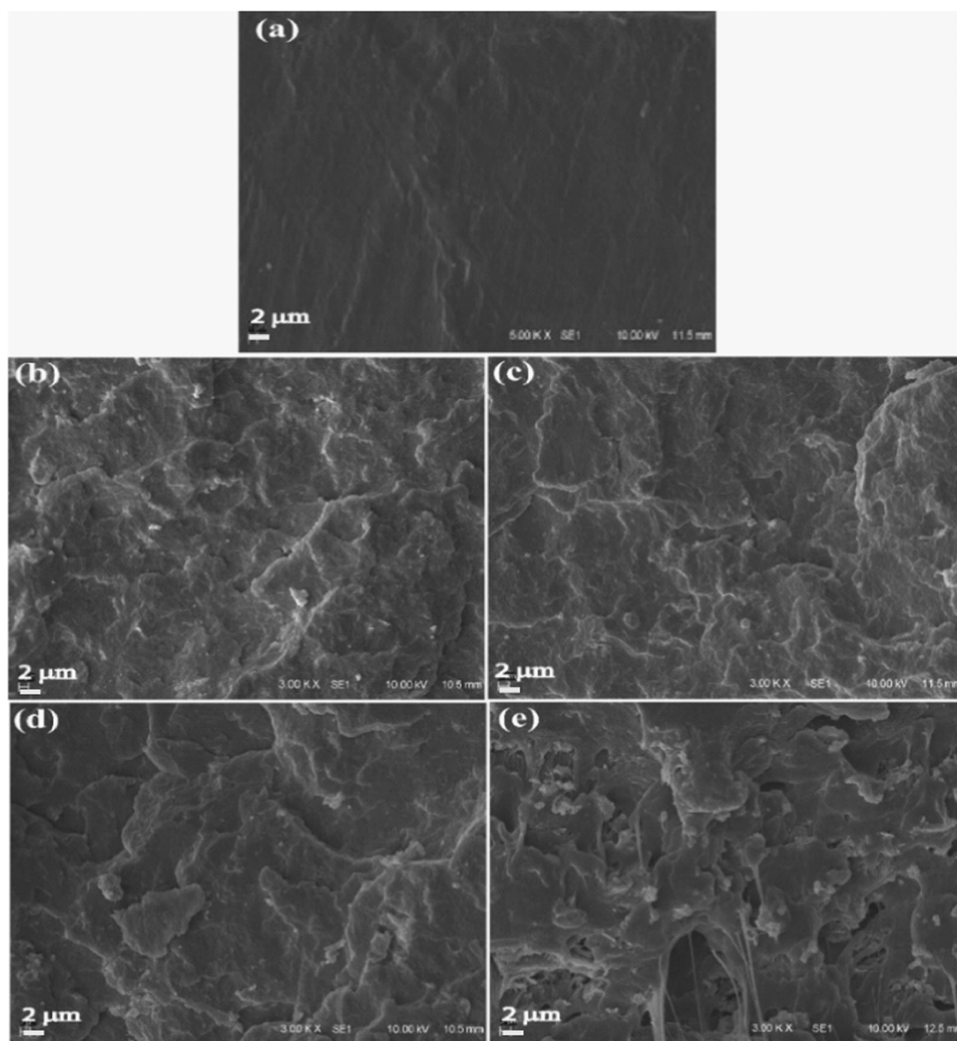
Figure 4. SEM images of pure PP (a), PP-TrGO$_{600}$-Co-5% (b), PP-TrGO$_{1000}$-Co-5% (c), PP-TrGO$_{600}$-Ni-5% (d), and TrGO$_{1000}$-Ni-5% (e).

and an increase in the oxygen percentage. This could be attributed to the formation of oxides of metallic nanoparticles. Furthermore, the BET surface area results of the nanomaterials are presented in Table 1. The analysis shows a significant enhancement in surface area from 70 m^{2}g^{-1} for GO to 283 and 373 m^{2}g^{-1} for TrGO$_{600}$ and TrGO$_{1000}$, respectively. These results prove the effectiveness of the thermal reduction in the exfoliation of GO. On the other hand, the support of metallic nanoparticles (Ni, Co) displays a substantial reduction in the total pore volume and surface area of TrGO, presenting maximum decreases of 48 and 65% for TrGO$_{600}$ and TrGO$_{1000}$, respectively. A similar decrease in the surface of TrGO with the support of metallic nanoparticles has been reported by other researchers.[34] The reduction in the surface area with the addition of metallic nanoparticles is perhaps due to the blockage of some pores by metallic nanoparticles during the synthesis as well as because of the coarsening effect.[51,52] The greater decrease in the surface area of TrGO$_{1000}$ compared to that of TrGO$_{600}$ is, most probably, a consequence of the accessibility of a large surface area for the support of the metallic particles, which in turn decreases the surface area.

Atomic absorption spectroscopy confirmed the presence of MNPs on the surface of TrGO. The results show the deposition of metallic particles ranging from 9 to 12% with a standard deviation of ±3, indicating the deposition of almost

similar amounts of Ni and Co nanoparticles. The deposition of similar amounts of MNPs in TrGOs, obtained at different reduction temperatures, could be due to two different phenomena operating during the support of the MNPs on carbon materials having different surface areas and chemical structures. The reduction at 600 °C left more polar functional groups on TrGO as compared to the reduction at 1000 °C, providing more interaction between the polar group and MNPs to be supported. On the other hand, TrGO$_{1000}$ (372 m^{2}g^{-1}) has a higher surface area available for the support of MNPs compared to TrGO$_{600}$ (282 m^{2}g^{-1}). Thus, the above two phenomena compete with each other, and finally, almost the same amounts of metallic particles are supported on the two surfaces. Thus, we concluded that the reduction of GO at two different temperatures (600 and 1000 °C) has no significant effect on the support of metallic nanoparticles.

To investigate the dispersion of the filler and the interfacial bonding between metal-supported TrGO and the PP matrix, scanning electron microscopy (SEM) images of the fracture interface were obtained, as displayed in Figure 4. The latter demonstrates the cross-sectional view of the samples, presenting a relatively rough morphology compared to that of neat PP [Figure 4a] because of the improved crystalline structure of PP. The strong layered morphology of PP composites reveals that the polymer is coated around the

Table 2. Thermal Properties of the Neat PP, PP-TrGO-Ni, and PP-TrGO-Co Nanocomposites

samples	filler (%)	residue (%)[a]	metal (%)[b]	T_{onset} (°C)	T_{max} (°C)	T_m	T_c	X_c (%)
Neat PP	0	0		412	455	163	107	38
PP-TrGO$_{600}$-Co	1.0	1.71	0.09	430	467	164	117	43
PP-TrGO$_{600}$-Co	3.0	2.95	0.27	431	463	164	118	46
PP-TrGO$_{600}$-Co	5.0	5.32	0.45	446	474	164	120	48
PP-TrGO$_{1000}$-Co	1.0	1.43	0.09	434	470	163	117	44
PP-TrGO$_{1000}$-Co	3.0	3.12	0.27	435	470	163	119	40
PP-TrGO$_{1000}$-Co	5.0	4.51	0.45	442	474	160	118	40
PP-TrGO$_{600}$-Ni	1.0	0.9	0.12	432	469	163	117	44
PP-TrGO$_{600}$-Ni	3.0	4.32	0.36	423	463	163	120	45
PP-TrGO$_{600}$-Ni	5.0	5.98	0.60	440	471	164	120	42
PP-TrGO$_{1000}$-Ni	1.0	1.28	0.08	435	470	163	115	51
PP-TrGO$_{1000}$-Ni	3.0	4.66	0.24	421	463	163	118	41
PP-TrGO$_{1000}$-Ni	5.0	5.52	0.40	441	473	165	120	40

[a]Calculated from the TGA residue. [b]Calculated from atomic absorption.
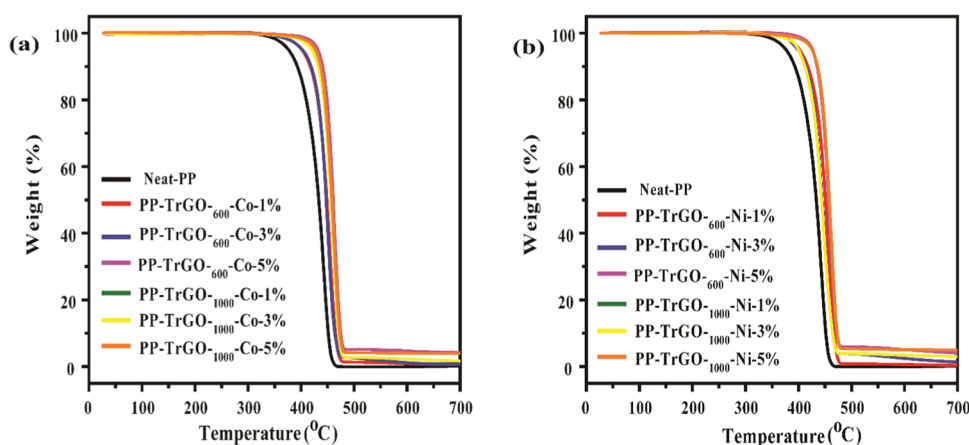

Figure 5. TGA thermograms of neat PP and PP-TrGO-Co nanocomposites (a) and neat PP and PP-TrGO-Ni nanocomposites (b).
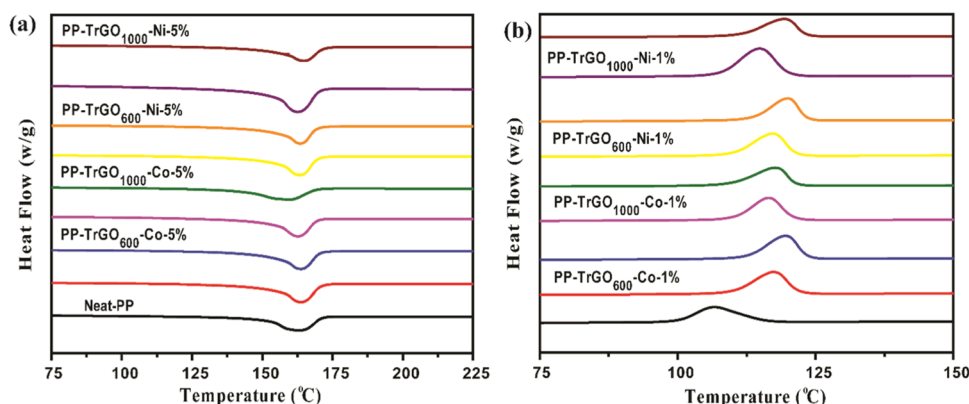

Figure 6. DSC thermograms of neat PP, PP-TrGO-Co and PP-TrGO-Ni nanocomposites (a) 5 wt % of filler (b) 1 wt % of filer.

fillers, enhancing the dispersion of the filler. The invisibility of the MNs confirms the uniform distribution in the PP matrix.

To evaluate the nature of the interaction between PP and metal-supported TrGO. An FT-IR study was conducted, and the results are illustrated in Figure 3b. The characteristic IR peaks of PP observed at 2950 and 2870 cm^{-1} correspond to the C−H asymmetric and C−H symmetric stretchings of CH$_3$ groups, respectively. The two peaks at 2918 and 2840 cm^{-1} are associated with the C−H symmetric stretching of CH$_2$ groups. Furthermore, the peaks at 1454, 1376, and 1167 cm^{-1} correspond to the asymmetric C−H bending vibration of

-CH$_2$ and CH$_3$ groups, symmetric C−H bending vibration of -CH$_2$ and CH$_3$ groups, and C−C stretching of C−CH$_3$ groups, respectively. A wide band around 3370 cm^{-1} related to hydroxyl groups and trapped water molecules in the graphene layer is also observed in PP-TrGO nanocomposites; the intensity of this peak is considerably low due to the low percentage of fillers in the polymer matrix.[3,53] To avoid the oxidation of the PP matrix, an antioxidant was used during melt mixing. The FT-IR spectra demonstrated the absence of the characteristic peak of C5O around 1720 cm^{-1}, showing that there is no oxidation taking place during melt mixing.
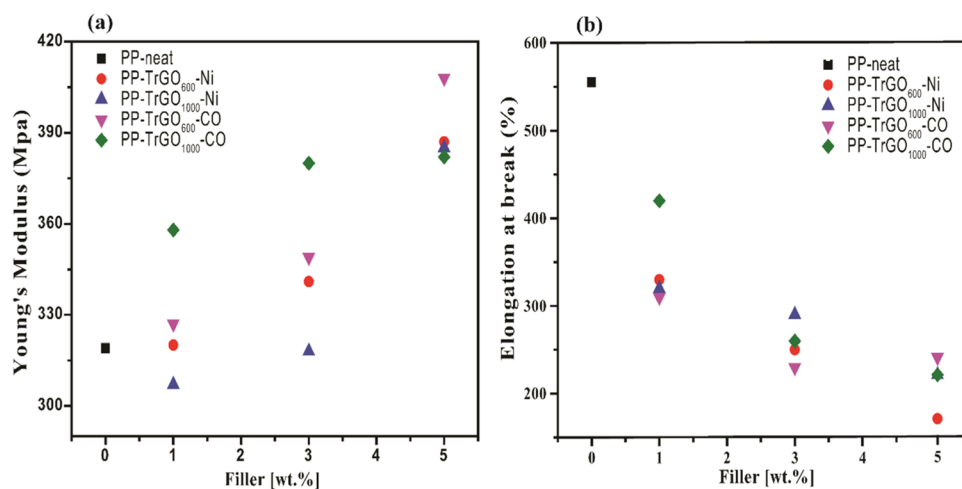
Figure 7. (a) Effect of the concentration of MNPs on the Young modulus and (b) elongation at break.

Figure 3b proves that with the addition of the filler, the sustainability of the chemical structure of PP was not altered, as it is clear from the characteristic PP spectrum. This proves the physical incorporation of the filler in the polymer rather than chemical linkage during nanocomposite blending.[54]

A summary of the thermal performance of the polymeric nanocomposites is given in Table 2 and Figures 5 and 6. It can be observed from Table 2 that with the incorporation of NPs, the initial (T_{onset}) and maximum (T_{max}) degradation temperatures of the nanocomposites increase with respect to those of neat PP. T_{onset} and T_{max} of the sample PP-TrGO$_{600}$-Co-5% show maximum increases of 34 and 19 °C, respectively, attaining the highest values of 446 and 474°C. The studies show that the introduction of graphene and its derivatives with a high aspect ratio and surface area in the polymer produces tortuous paths, hindering gas molecule diffusion and causing a remarkable reduction in the permeation quantity of gas.[55] Herein, TrGO serves as a physical barrier preventing the transfer of oxygen molecules to the degradation sites of the polymer, delaying the volatilization of the generated macroradical, and enhancing the thermal stability.[56]

Interestingly, all samples with 1.0 and 5.0 wt % fillers present superior thermal stability than those with 3.0 wt % fillers. The cause for the decline in the thermal behavior of the composites as the addition of fillers is increased from 1.0 to 3.0 wt % is not clear. However, various authors have reported the effect of metallic NPs, including Ni, Cu, Co, Fe, and Al, on the thermal degradation of polymers such as LDPE, HDPE, and PP. They considered that the catalytic effect of the metal is responsible for the thermal behavior of the organic segment of the polymers at changeable rates.[57] For the TrGO-Co and TrGO-Ni nanoparticles studied in the present work, Co and Ni are supposed to be protected by the carbon part of graphene oxide, preventing the direct interaction of metallic nanoparticles with PP, thus avoiding catalytic thermal degradation. However, the availability of a small amount of metal is possible, which could lower the thermal stability by competing for the carbon part.

Furthermore, DSC analysis of the pristine PP, PP-TrGO-Co, and PP-TrGO-Ni nanocomposites was carried out to obtain information about the percent crystallinity along with the melting and crystallization temperatures. It can be seen in Figure 6a that the introduction of the filler did not modify the melting temperature (T_m) prominently. However, the employment of TrGO-based fillers increases the crystallization

temperature (Figure 6b), indicating that the filler functions as a seed for rapid nucleation. The observed nucleation result was more prominent at higher amounts of filler loadings, i.e., 5.0 wt % (see Table 2); these findings reveal that a higher quantity of NPs causes an increase in the heterogenous nucleation effect, which favors the formation of more crystals.[58,59] Higher T_c values promote a reduced processing cycle and increase the production rate.[52] Likewise, the percent crystallinity (X_c) shows a maximum of 13% improvement compared to that of pure PP. This indicates that the crystallization rather begins at a higher temperature with the development of bigger/improved crystals enhancing the T_c and X_c of the nanocomposites compared to that of neat PP.

Typically, the composite materials present advanced mechanical properties with the incorporation of a definite amount of fillers. However, critical factors such as the aspect ratio, dispersion, surface area, polymer–filler interaction, and the crystalline structure of the polymer greatly affect the mechanical properties of the polymeric materials.[54] Figure 7a displays the variation in the tensile modulus with respect to the filler addition. It can be noted that the PP reinforced filler nanocomposites show an improved tensile modulus as compared to bare PP. As the amount of TrGO-supported metallic nanoparticles is increased in the polymer, the Young's modulus shows a gradual improvement. Practically, all samples with filler addition show an enhanced modulus of elasticity; however, the sample PP-TrGO-$_{600}$-Co-5% demonstrates a maximum enhancement of 27% compared to neat PP. This enhancement in mechanical properties of the nanocomposites is credited to the exfoliated nature of TrGO with increased specific surface area in interaction with the PP matrix, improving the load transfer from PP to TrGO and improved interfacial contact between the filler and the polymer matrix.[60] Alternately, the elongation at break value decreases with the incorporation of a higher amount of the filler, as can be seen in Figure 7b. This effect is well understood as with the introduction of TrGO, the motion of the PP chain becomes limited, and the polymer matrix converts into a more rigid one, as shown in other studies.[61−63]

For the practical application of the polymer nanocomposites, it is imperative to assess the water wettability of the composite materials, practically estimated by the water contact angle (θ) measurement. The water contact angle measurement in the present work does not show a clear trend. However, some of

the samples can be considered as hydrophilic in nature compared to neat PP, presenting a water contact angle value lower than 90°, as shown in Figure 8.[64] All of the samples
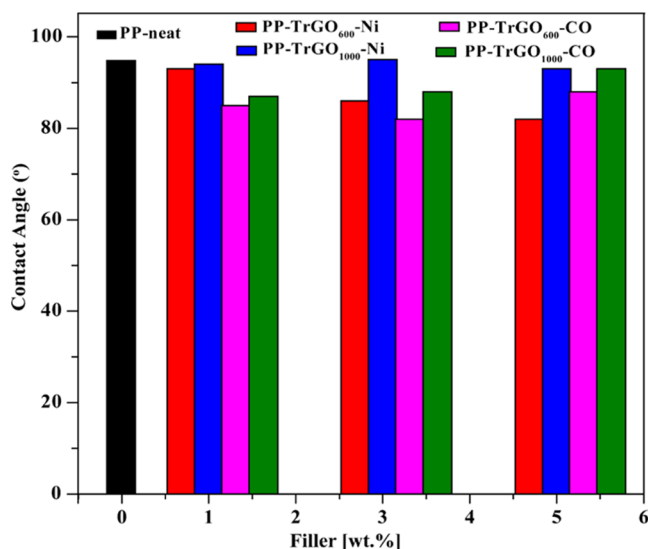

Figure 8. Results of the water contact angle of the bare PP and nanocomposites with different filler percentages.

containing $TrGO_{1000}$-Ni show almost identical θ values compared to neat PP; the rest of the samples demonstrated a rather lower θ value with the loading of the metal-supported TrGO nanoparticles. Interestingly, it can be noted that the PP-TrGO-600-Ni/or Co samples show a lower contact angle than PP-TrGO-1000-Ni/or Co for all concentrations of the filler used. This can be due to the fact that the GO reduced at 600 °C contains more polar groups than the GO reduced at 1000 °C, which interact more strongly with water molecules. A literature research showed that the incorporation of fillers such as clay, carbon nanotubes, and graphene oxide can produce an increase in the hydrophilic behavior of polymer nano-composites.[65−67]

5. MAGNETIC CHARACTERIZATION

Figure 9 presents the variations of the magnetization, M, with the magnetic field $M(H)$ measured for Co and Ni nano-particles supported on the thermally reduced (at 600 and 1000 °C) graphene oxide. The maximum field applied here is high enough to avoid any minor loop effects.[68−70] Both Co and Ni nanoparticles supported on $TrGO_{600}$ show the typical behavior for very small superparamagnetic particles with $M(H)$ having very low coercivity, H_C, values of 8 and 11 Oe, respectively. On the other hand, nanoparticles supported on $TrGO_{1000}$, although still predominantly superparamagnetic, present hysteresis loops with higher H_C values of 60 and 90 Oe for the Co and Ni samples, respectively. This increase indicates the presence of a small portion of particles (or agglomerations) with sufficiently large sizes to exhibit ferromagnetic behavior. Also, the overall superparamagnetic shape of the $M(H)$ curves for the latter samples is characteristic of systems that are larger in size, as compared with the former ones, nanoparticles.

The magnetization hysteresis loops, traced for the PP-TrGO-Co and PP-TrGO-Ni nanocomposites with 1 and 5 wt % fillers, are plotted in Figure 10. The pertinent parameters extracted from the magnetization data corresponding to the samples with 3 wt % fillers presented values in between those of the samples with 1 and 5 wt % fillers. Thus, for better visualization, magnetization curves for samples with 3 wt % fillers are not displayed in Figure 10. Although all curves in this figure are characteristic of ferromagnetic systems and seem rather comparable in shape, the low-field $M(H)$ slopes of the PP-TrGO-Ni nanocomposites are apparently higher. Also, all Co samples show normalized remanent magnetization values (∼0.04), approximately half that (∼0.10) of the respective Ni samples. The H_C values vary slightly, between ∼60 and ∼90 Oe, for all samples, always being higher for the Ni samples. The above features indicate that, most probably, the PP-TrGO-Co nanocomposites have a higher ratio of super-paramagnetic and ferromagnetic fractions.

Here, we also estimated the effects of the magnetic interactions in all samples with the help of the recoil loop δM_R plots technique[71] based on a relationship between parts of a recoil magnetization hysteresis loop, which is used to build an δM_R plot. For uniaxial magnetic anisotropy systems, it is
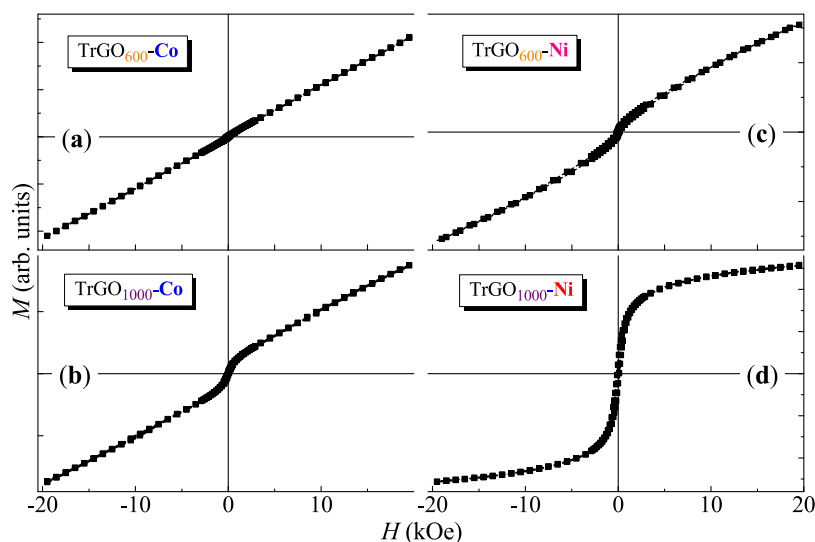

Figure 9. Magnetization versus magnetic field variations obtained for the TrGO-supported Co (a and b) and Ni (c and d) nanoparticles.
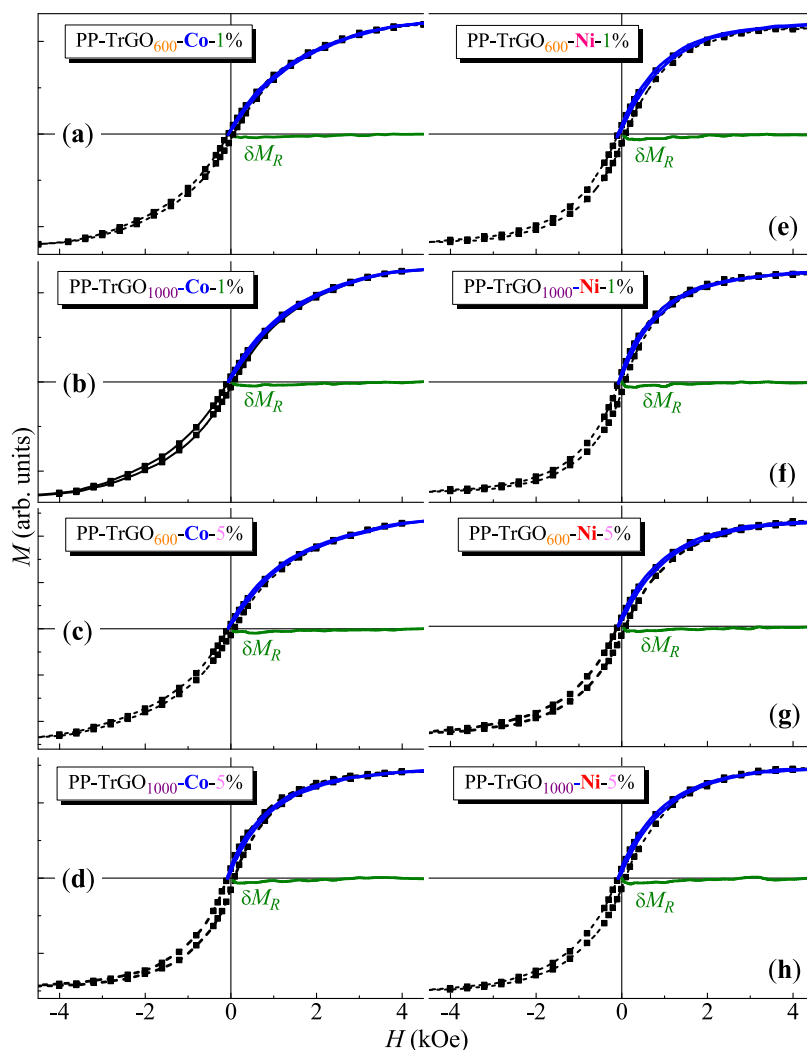
Figure 10. Magnetization hysteresis loops (symbols), recoil loops (solid curves), and the respective δM_R plots, measured for the PP-TrGO-Co (a−d) and PP-TrGO-Ni (e−h) nanocomposites.

accepted that nonzero deviations of $\delta M_R(H)$ are caused by magnetic interactions. In the present work, δM_R plots were constructed from recoil loops with a recoil branch starting at a field approximately equal to H_C. The respective recoil curves and the δM_R plots obtained from them are also displayed in Figure 10. All δM_R plots show very small negative values, indicating that the interactions present are very weak and of dipolar type. This implies that in each sample, the ferromagnetic metallic nanoparticles are uniformly distributed and do not aggregate significantly.

6. CONCLUSIONS

The development of magnetic materials for microelectronic applications is an emerging area of research. Here, we report the synthesis of thermally stable PP magnetic nanocomposites using reduced graphene oxide-supported Ni and Co NPs. The synthesis process of the nanofiller leads to the encapsulation of the magnetic particles by the carbon portion, shielding them from oxidation and providing protection, thus enhancing their distribution in the polymer by hindering magnetically induced agglomeration. Atomic absorption spectroscopy confirms that similar amounts of metal nanoparticles were supported on the TrGO reduced at 600 and 1000 °C. The FT-IR spectra

confirm the characteristic bands for GO and TrGO and also confirm the chemical structure of PP. The uniform diffusion of the filler in the PP matrix is established by SEM analysis. The thermal analysis of the nanocomposites indicates an enhancement of T_{onset} and T_{max} with the addition of the filler. The DSC analysis indicates an improvement of 13° in the value of T_c, while X_c increases from 38 to 51% in comparison to that of pristine PP. The filler addition enhances the modulus of elasticity, making some of the samples hydrophilic. Interestingly, with the inclusion of a magnetic filler, the polymer matrix shows a ferromagnetic behavior at room temperature. These findings are substantial given that most of the studies described in the literature reveal better magnetic characteristics at low temperatures, while here, we report a rather high coercivity value of ∼90 Oe at room temperature. Therefore, the multifunctional flexible magnetic materials reported here present a variety of possible applications with potential processability, for instance, in electromagnetic device applications, microelectronics, and aircraft industries.

■ AUTHOR INFORMATION

Corresponding Authors

Muhammad Nisar − *Facultad de Ingeniería, Universidad Católica de la Santísima Concepción, Concepción 4090541,*

Chile; ● orcid.org/0000-0002-1305-5188;
Email: mnisar@ucsc.cl

Raúl Quijada − *Departamento de Ingeniería Química, Biotecnología y Materiales, Facultad de Ciencias Físicas y Matemáticas, Santiago 8370456, Chile*; Email: raquijad@ing.uchile.cl

Authors

Griselda Barrera Galland − *Instituto de Química, Universidade Federal do Rio Grande do Sul, 91501-970 Porto Alegre, Brazil*; ● orcid.org/0000-0003-3678-9106

Julian Geshev − *Instituto de Física, Universidade Federal do Rio Grande do Sul, 91501-970 Porto Alegre, Brazil*

Carlos Bergmann − *Laboratório de Materiais Cerâmicos, Departamento de Materiais, Universidade Federal do Rio Grande do Sul, Porto Alegre 90010-150, Brazil*

Complete contact information is available at:
https://pubs.acs.org/10.1021/acsomega.3c01917

Notes

■ ACKNOWLEDGMENTS

■ REFERENCES

(1) Jazzar, A.; Alamri, H.; Malajati, Y.; Mahfouz, R.; Bouhrara, M.; Fihri, A. Recent Advances in the Synthesis and Applications of Magnetic Polymer Nanocomposites. *J. Ind. Eng. Chem.* **2021**, *99*, 1−18.

(2) Idumah, C. I.; Hassan, A. Emerging Trends in Graphene Carbon Based Polymer Nanocomposites and Applications. *Rev. Chem. Eng.* **2016**, *32*, 223−264.

(3) Sánchez-Valdes, S.; Zapata-Domínguez, A. G.; Martinez-Colunga, J. G.; Mendez-Nonell, J.; Ramos de Valle, L. F.; Espinoza-Martinez, A. B.; Morales-Cepeda, A.; Lozano-Ramirez, T.; Lafleur, P. G.; Ramirez-Vargas, E. Influence of Functionalized Polypropylene on Polypropylene/Graphene Oxide Nanocomposite Properties. *Polym. Compos.* **2018**, *39*, 1361−1369.

(4) Constant-Mandiola, B.; Aguilar-Bolados, H.; Geshev, J.; Quíjada, R. Study of the Influence of Magnetite Nanoparticles Supported on Thermally Reduced Graphene Oxide as Filler on the Mechanical and Magnetic Properties of Polypropylene and Polylactic Acid Nanocomposites. *Polymers* **2021**, *13*, 1635.

(5) Dashairya, L.; Rout, M.; Saha, P. Reduced Graphene Oxide-Coated Cotton as an Efficient Absorbent in Oil-Water Separation. *Adv. Compos. Hybrid Mater.* **2018**, *1*, 135−148.

(6) Cui, Y.; Kundalwal, S. I.; Kumar, S. Gas Barrier Performance of Graphene/Polymer Nanocomposites. *Carbon* **2016**, *98*, 313−333.

(7) Lee, C.; Wei, X.; Kysar, J. W.; Hone, J. Measurement of the Elastic Properties and Intrinsic Strength of Monolayer Graphene. *Science* **2008**, *321*, 385−388.

(8) Su, T.; Shao, Q.; Qin, Z.; Guo, Z.; Wu, Z. Role of Interfaces in Two-Dimensional Photocatalyst for Water Splitting. *ACS Catal.* **2018**, *8*, 2253−2276.

(9) Balandin, A. A.; Ghosh, S.; Bao, W.; Calizo, I.; Teweldebrhan, D.; Miao, F.; Lau, C. N. Superior Thermal Conductivity of Single-Layer Graphene. *Nano Lett.* **2008**, *8*, 902−907.

(10) Gibson, R. F. A Review of Recent Research on Mechanics of Multifunctional Composite Materials and Structures. *Compos. Struct.* **2010**, *92*, 2793−2810.

(11) Stankovich, S.; Dikin, D. A.; Dommett, G. H. B.; Kohlhaas, K. M.; Zimney, E. J.; Stach, E. A.; Piner, R. D.; Nguyen, S. B. T.; Ruoff, R. S. Graphene-Based Composite Materials. *Nature* **2006**, *442*, 282−286.

(12) Kim, H.; Abdala, A. A.; MacOsko, C. W. Graphene/Polymer Nanocomposites. *Macromolecules* **2010**, *43*, 6515−6530.

(13) Lerf, A.; He, H.; Forster, M.; Klinowski, J. Structure of Graphite Oxide Revisited. *J. Phys. Chem. B* **1998**, *102*, 4477−4482.

(14) Cheng, S.; Chen, X.; Hsuan, Y. G.; Li, C. Y. Reduced Graphene Oxide-Induced Polyethylene Crystallization in Solution and Nanocomposites. *Macromolecules* **2012**, *45*, 993−1000.

(15) de Oliveira, Y. D. C.; Amurin, L. G.; Valim, F. C. F.; Fechine, G. J. M.; Andrade, R. J. E. The Role of Physical Structure and Morphology on the Photodegradation Behaviour of Polypropylene-Graphene Oxide Nanocomposites. *Polymer (Guildf).* **2019**, *176*, 146−158.

(16) Kim, H.; Macosko, C. W. Processing-Property Relationships of Polycarbonate/Graphene Composites. *Polymer* **2009**, *50*, 3797−3809.

(17) Thomassin, J. M.; Trifkovic, M.; Alkarmo, W.; Detrembleur, C.; Jérôme, C.; Macosko, C. Poly(Methyl Methacrylate)/Graphene Oxide Nanocomposites by a Precipitation Polymerization Process and Their Dielectric and Rheological Characterization. *Macromolecules* **2014**, *47*, 2149−2155.

(18) Kim, H.; Miura, Y.; MacOsko, C. W. Graphene/Polyurethane Nanocomposites for Improved Gas Barrier and Electrical Conductivity. *Chem. Mater.* **2010**, *22*, 3441−3450.

(19) Kim, H. M.; Lee, J. K.; Lee, H. S. Transparent and High Gas Barrier Films Based on Poly(Vinyl Alcohol)/Graphene Oxide Composites. *Thin Solid Films* **2011**, *519*, 7766−7771.

(20) Long, J.; Li, S.; Liang, J.; Wang, Z.; Liang, B. Preparation and Characterization of Graphene Oxide and It Application as a Reinforcement in Polypropylene Composites. *Polym. Compos.* **2019**, *40*, 723−729.

(21) Huang, C.-L.; Lou, C.; Liu, C.; Huang, C.; Song, X.; Lin, J. Polypropylene/Graphene and Polypropylene/Carbon Fiber Conductive Composites: Mechanical, Crystallization and Electromagnetic Properties. *Appl. Sci.* **2015**, *5*, 1196−1210.

(22) Tang, S. C. N.; Lo, I. M. C. Magnetic Nanoparticles: Essential Factors for Sustainable Environmental Applications. *Water Res.* **2013**, *47*, 2613−2632.

(23) Neamtu, M.; Nadejde, C.; Hodoroaba, V. D.; Schneider, R. J.; Verestiuc, L.; Panne, U. Functionalized Magnetic Nanoparticles: Synthesis, Characterization, Catalytic Application and Assessment of Toxicity. *Sci. Rep.* **2018**, *8*, No. 6278.

(24) Hasan, A.; Morshed, M.; Memic, A.; Hassan, S.; Webster, T. J.; Marei, H. E. S. Nanoparticles in Tissue Engineering: Applications, Challenges and Prospects. *Int. J. Nanomedicine* **2018**, *Volume 13*, 5637−5655.

(25) Ito, A.; Shinkai, M.; Honda, H.; Kobayashi, T. Medical Application of Functionalized Magnetic Nanoparticles. *J. Biosci. Bioeng.* **2005**, *100*, 1−11.

(26) Tran, N.; Webster, T. J. Magnetic Nanoparticles: Biomedical Applications and Challenges. *J. Mater. Chem.* **2010**, *20*, 8760−8767.

(27) Saleh, K.; Guigon, P. Chapter 7 Coating and Encapsulation Processes in Powder Technology. *Handb. Powder Technol.* **2007**, *11*, 323−375.

(28) Zhu, N.; Ji, H.; Yu, P.; Niu, J.; Farooq, M. U.; Akram, M. W.; Udego, I. O.; Li, H.; Niu, X. Surface Modification of Magnetic Iron Oxide Nanoparticles. *Nanomaterials* **2018**, *8*, 810.

(29) Guo, T.; Lin, M.; Huang, J.; Zhou, C.; Tian, W.; Yu, H.; Jiang, X.; Ye, J.; Shi, Y.; Xiao, Y.; Bian, X.; Feng, X. The Recent Advances of Magnetic Nanoparticles in Medicine. *J. Nanomater.* **2018**, *2018*, 1.

(30) Neamtu, J.; Jitaru, I.; Malaeru, T.; Georgescu, G.; Kappel, W.; Alecu, V. Synthesis and Properties of Magnetic Nanoparticles with Potential Applications in Cancer Diagnostic. *Preparation of Metallic Nanoparticles*, 2005; Vol *1*, pp 222−4.

(31) Barrera, G.; Tiberto, P.; Allia, P.; Bonelli, B.; Esposito, S.; Marocco, A.; Pansini, M.; Leterrier, Y. Magnetic Properties of Nanocomposites. *Appl. Sci.* **2019**, *9*, 212.

(32) Zaaba, N. I.; Foo, K. L.; Hashim, U.; Tan, S. J.; Liu, W. W.; Voon, C. H. Synthesis of Graphene Oxide Using Modified Hummers Method: Solvent Influence. *Procedia Eng.* **2017**, *184*, 469−477.

(33) Botas, C.; Álvarez, P.; Blanco, C.; Santamaría, R.; Granda, M.; Gutiérrez, M. D.; Rodríguez-Reinoso, F.; Menéndez, R. Critical Temperatures in the Synthesis of Graphene-like Materials by Thermal Exfoliation-Reduction of Graphite Oxide. *Carbon* **2013**, *52*, 476−485.

(34) Bhowmik, K.; Mukherjee, A.; Mishra, M. K.; De, G. Stable Ni Nanoparticle-Reduced Graphene Oxide Composites for the Reduction of Highly Toxic Aqueous Cr(VI) at Room Temperature. *Langmuir* **2014**, *30*, 3209−3216.

(35) Resano, M.; Bolea-Fernández, E.; Mozas, E.; Flórez, M. R.; Grinberg, P.; Sturgeon, R. E. Simultaneous Determination of Co, Fe, Ni and Pb in Carbon Nanotubes by Means of Solid Sampling High-Resolution Continuum Source Graphite Furnace Atomic Absorption Spectrometry. *J. Anal. At. Spectrom.* **2013**, *28*, 657−665.

(36) Oliveira, A. E. F.; Braga, G. B.; Tarley, C. R. T.; Pereira, A. C. Thermally Reduced Graphene Oxide: Synthesis, Studies and Characterization. *J. Mater. Sci.* **2018**, *53*, 12005−12015.

(37) Nekahi, A.; Marashi, P. H.; Haghshenas, D. Applied Surface Science Transparent Conductive Thin Film of Ultra Large Reduced Graphene Oxide Monolayers. *Appl. Surf. Sci.* **2014**, *295*, 59−65.

(38) Davar, F.; Fereshteh, Z.; Salavati-Niasari, M. Nanoparticles Ni and NiO: Synthesis, Characterization and Magnetic Properties. *J. Alloys Compd.* **2009**, *476*, 797−801.

(39) Scherrer, P. Bestimmung Der Grösse Und Der Inneren Struktur von Kolloidteilchen Mittels Röntgenstrahlen. *Nachr. Ges. Wiss. Göttingen, Math.-Phys. Kl.* **1918**, *26*, 98.

(40) Tariq, M.; Haq, S. ul.; Ahsan, A.; Syed, W. A. Using Cobalt and Nickel Oxide Nanoparticles for the Conversion of Solid Kitchen Waste into Biofuel. *Curr. Anal. Energy Environ. Sci.* **2019**, *1*, 26−29.

(41) Hernandez, Y.; Nicolosi, V.; Lotya, M.; Blighe, F. M.; Sun, Z.; De, S.; McGovern, I. T.; Holland, B.; Byrne, M.; Gun'ko, Y. K.; Boland, J. J.; Niraj, P.; Duesberg, G.; Krishnamurthy, S.; Goodhue, R.; Hutchison, J.; Scardaci, V.; Ferrari, A. C.; Coleman, J. N. High-Yield Production of Graphene by Liquid-Phase Exfoliation of Graphite. *Nat. Nanotechnol.* **2008**, *3*, 563−568.

(42) Shen, Q.; Yang, J.; Chen, K. L.; Wang, H.; Liu, J. B.; Yan, H. Co3O4 Nanorods−Graphene Composites as Catalysts for Rechargeable Zinc-Air Battery. *J. Solid State Electrochem.* **2016**, *20*, 3331−3336.

(43) Zhang, X.; Li, K.; Li, H.; Lu, J.; Fu, Q.; Zhang, L. Hydrothermal Synthesis of Cobalt Oxide Porous Nanoribbons Anchored with Reduced Graphene Oxide for Hydrogen Peroxide Detection. *J. Nanoparticle Res.* **2016**, *18*, 1−12.

(44) Madhura, T. R; kumar, G. G.; Ramaraj, R. Reduced Graphene Oxide Supported 2D-NiO Nanosheets Modified Electrode for Urea Detection. *J. Solid State Electrochem.* **2020**, *24*, 3073−3081.

(45) Dao, V. D.; Larina, L. L.; Jung, K. D.; Lee, J. K.; Choi, H. S. Graphene-NiO Nanohybrid Prepared by Dry Plasma Reduction as a Low-Cost Counter Electrode Material for Dye-Sensitized Solar Cells. *Nanoscale* **2014**, *6*, 477−482.

(46) Gao, J. S.; Lian, T.; Liu, Z.; He, Y. Efficient NiO/RGO Combination for High-Cycling-Stability Supercapacitors by an Alkaline Hydrothermal Strategy. *J. Appl. Electrochem.* **2022**, *52*, 1045−1052.

(47) Zhu, H.; Zeng, X.; Han, T.; Li, X.; Zhu, S.; Sun, B.; Zhou, P.; Liu, J. A Nickel Oxide Nanoflakes/Reduced Graphene Oxide Composite and Its High-Performance Lithium-Storage Properties. *J. Solid State Electrochem.* **2019**, *23*, 2173−2180.

(48) Emiru, T. F.; Worku, D. Egyptian Journal of Basic and Applied Sciences Controlled Synthesis, Characterization and Reduction of Graphene Oxide: A Convenient Method for Large Scale Production. *Egypt. J. Basic Appl. Sci.* **2017**, *4*, 74−79.

(49) Andrijanto, E.; Shoelarta, S.; Subiyanto, G.; Rifki, S. *Facile Synthesis of Graphene from Graphite Using Ascorbic Acid as Reducing Agent Facile Synthesis of Graphene from Graphite Using Ascorbic Acid as Reducing Agent. AIP Conference Proceedings*, 2018; p 1725.

(50) Saleem, H.; Haneef, M.; Abbasi, H. Y. Synthesis Route of Reduced Graphene Oxide via Thermal Reduction of Chemically Exfoliated Graphene Oxide. *Mater. Chem. Phys.* **2018**, *204*, 1−7.

(51) Ndolomingo, M. J.; Meijboom, R. Kinetics of the Catalytic Oxidation of Morin on γ-Al2O3 Supported Gold Nanoparticles and Determination of Gold Nanoparticles Surface Area and Sizes by Quantitative Ligand Adsorption. *Appl. Catal., B* **2016**, *199*, 142−154.

(52) Kou, R.; Shao, Y.; Mei, D.; Nie, Z.; Wang, D.; Wang, C.; Viswanathan, V. V.; Park, S.; Aksay, I. A.; Lin, Y.; Wang, Y.; Liu, J. Stabilization of Electrocatalytic Metal Nanoparticles at Metal-Metal Oxide-Graphene Triple Junction Points. *J. Am. Chem. Soc.* **2011**, *133*, 2541−2547.

(53) Ryu, S. H.; Shanmugharaj, A. M. Influence of Hexamethylene Diamine Functionalized Graphene Oxide on the Melt Crystallization and Properties of Polypropylene Nanocomposites. *Mater. Chem. Phys.* **2014**, *146*, 478−486.

(54) Nisar, M.; Thue, P. S.; Maghous, M. B.; Geshev, J.; Lima, E. C.; Einloft, S. Metal Activated Carbon as an Efficient Filler for High-Density Polyethylene Nanocomposites. *Polym. Compos.* **2020**, *41*, 3184−3193.

(55) Yuan, B.; Bao, C.; Song, L.; Hong, N.; Liew, K. M.; Hu, Y. Preparation of Functionalized Graphene Oxide/Polypropylene Nanocomposite with Significantly Improved Thermal Stability and Studies on the Crystallization Behavior and Mechanical Properties. *Chem. Eng. J.* **2014**, *237*, 411−420.

(56) Lu, H.; Hu, Y.; Li, M.; Chen, Z.; Fan, W. Structure Characteristics and Thermal Properties of Silane-Grafted-Polyethylene/Clay Nanocomposite Prepared by Reactive Extrusion. *Compos. Sci. Technol.* **2006**, *66*, 3035−3039.

(57) Nisar, M.; Thue, P. S.; Heck, C. A.; Salazar Cuaila, J. L.; Geshev, J.; Lima, E. C.; Jacobi, M. M.; Galland, G. B. Synthesis of Polyethylene/Nickel−Carbon Stimuli-Responsive Material under Magnetic Field at Room Temperature: Effect of the Filler on the Properties. *Eur. Polym. J.* **2018**, *99*, 378−383.

(58) Nisar, M.; Sebag Bernd, M. d. G.; Pinto da Silva Filho, L. C.; Geshev, J.; Barrera Galland, G. Polypropylene/Carbon Nanotube Magnetic Composites Obtained Using Carbon Nanotubes from Sawdust. *Polym. Adv. Technol.* **2019**, *30*, 457−464.

(59) Gopakumar, T. G.; Pagé, D. J. Y. S. Polypropylene/Graphite Nanocomposites by Thermo-Kinetic Mixing. *Polym. Eng. Sci.* **2004**, *44*, 1162−1169.

(60) Lee, S. J.; Yoon, S. J.; Jeon, I. Graphene/Polymer Nanocomposites: Preparation, Mechanical Properties, and Application. *Polymers* **2022**, *14*, 4733.

(61) Bagheriasl, D.; Carreau, P. J.; Dubois, C.; Riedl, B. Properties of Polypropylene and Polypropylene / Poly (Ethylene-Co- Vinyl Alcohol) Blend / CNC Nanocomposites. *Compos. Sci. Technol.* **2015**, *117*, 357−363.

(62) Kim, S.; Lee, S. W.; Lee, Y.; Lee, J.; et al. Improving Physical Properties of Polypropylene Nanocomposites by a Natural Resource-Based Bottom-up Graphene Oxide Filler. *Macromol. Res.* **2021**, *29*, 487−493.

(63) Kong, S.; Seo, H.; Shin, H.; Baik, J.; Oh, J.; Kim, Y.; Lee, J. Improvement in Mechanical and Thermal Properties of Polypropylene Nanocomposites Using an Extremely Small Amount of Alkyl Chain-Grafted Hexagonal Boron Nitride Nanosheets. *Polymer* **2019**, *180*, No. 121714.

(64) Díez-Pascual, A. M.; Díez-Vicente, A. L. Poly(Propylene Fumarate)/Polyethylene Glycol-Modified Graphene Oxide Nanocomposites for Tissue Engineering. *ACS Appl. Mater. Interfaces* **2016**, *8*, 17902−17914.

(65) Anadão, P.; Sato, L. F.; Wiebeck, H.; Valenzuela-Díaz, F. R. Montmorillonite as a Component of Polysulfone Nanocomposite Membranes. *Appl. Clay Sci.* **2010**, *48*, 127−132.

(66) Yang, Z.; Peng, H.; Wang, W.; Liu, T. Crystallization Behavior of Poly(ε-Caprolactone)/Layered Double Hydroxide Nanocomposites. *J. Appl. Polym. Sci.* **2010**, *116*, 2658−2667.

(67) Ganesh, B. M.; Isloor, A. M.; Ismail, A. F. Enhanced Hydrophilicity and Salt Rejection Study of Graphene Oxide-Polysulfone Mixed Matrix Membrane. *Desalination* **2013**, *313*, 199−207.

(68) Geshev, J.; Pereira, L. G.; Skumryev, V. Comment on "Exchange Bias Dependence on Interface Spin Alignment in a Ni80Fe20/(Ni,Fe)O Thin Film. *Phys. Rev. Lett.* **2008**, *100*, 97204.

(69) Geshev, J. Comment on "exchange Bias in the Layered Cobaltite Sr 1.5Pr0.5CoO4 " [J. Appl. Phys. 104, 023914 (2008)]. *J. Appl. Phys.* **2009**, *105*, 066108.

(70) Harres, A.; Mikhov, M.; Skumryev, V.; Andrade, A. M. H.; De; Schmidt, J. E.; Geshev, J. Journal of Magnetism and Magnetic Materials Criteria for Saturated Magnetization Loop. *J. Magn. Magn. Mater.* **2016**, *402*, 76−82.

(71) Geshev, J. Interaction Plots Obtained from In-Field Magnetization Instead of Remanence Measurements. *J. Magn. Magn. Mater.* **2018**, *467*, 135−138.

📖 Recommended by ACS

Fabrication of Superparamagnetic Bimetallic Magnesium Nanoferrite Using Green Polyol: Characterization and Anticancer Analysis in Vitro on Lung Cancer Cell Line A549

Rangnath Ravi, Sharif Ahmad, *et al.*

NOVEMBER 03, 2022
ACS APPLIED BIO MATERIALS   READ 🔗

Magnetic-Field-Induced Vapor-Phase Polymerization to Achieve PEDOT-Decorated Porous Fe_3O_4 Particles as Excellent Microwave Absorbers

Mingtao Qiao, Xiaorong Meng, *et al.*

AUGUST 26, 2022
INDUSTRIAL & ENGINEERING CHEMISTRY RESEARCH   READ 🔗

Comprehensive Study on the Reinforcement of Electrospun PHB Scaffolds with Composite Magnetic Fe_3O_4–rGO Fillers: Structure, Physico-Mechanical Properties, and Pi...

Artyom S. Pryadko, Maria A. Surmeneva, *et al.*

NOVEMBER 04, 2022
ACS OMEGA   READ 🔗

Electromagnetic Performance of NiMgCuZn Ferrite for Hyperthermia Application in Cancer Treatment

Xinliang Ge, Yang Zhang, *et al.*

MAY 04, 2023
ACS OMEGA   READ 🔗

Get More Suggestions >